Effect of the fuel on physical characteristics, optical properties and photocatalytic activity of solution combustion synthesised TiO_2 and black TiO_2

Pooja Philip[1], Sooboo Singh[1], Holger B. Friedrich[1] and Abdul S. Mahomed[1]*

[1]*Discipline of Chemistry, University of KwaZulu-Natal, Durban, South Africa.*

ABSTRACT

Titanium dioxide (TiO_2) photocatalysts were synthesised via the solution combustion synthesis (SCS) method using citric acid, urea, ethylene glycol, and glycine as fuels. Following optimisation, the urea-derived TiO_2 was subjected to hydrogen reduction under varying treatment conditions to produce black titania. The prepared materials were characterised using Fourier-transform infrared spectroscopy (FTIR), X-ray diffraction (XRD), high-resolution transmission electron microscopy (HRTEM), scanning electron microscopy (SEM), nitrogen physisorption, UV–visible diffuse reflectance spectroscopy (UV–Vis DRS), and photoluminescence (PL) spectroscopy. Photocatalytic activity was evaluated through the degradation of methylene blue (MB) under UV and UV–visible irradiation. Among the synthesised photocatalysts, the urea-derived TiO_2 exhibited the most favourable physicochemical properties, including highest surface area, lowest PL intensity and highest hydroxyl group density. These characteristics resulted in superior photocatalytic activity for MB degradation under both UV and UV–visible light. Following H_2 reduction of U-TiO_2, to form black titania, photocatalytic testing demonstrated significantly enhanced activity compared to the unreduced material. The findings highlight the effectiveness of using urea as fuel for SCS synthesised TiO_2 and hydrogen treatment of the material to improve structural and photocatalytic properties.

KEYWORDS

TiO_2, solution combustion, photocatalysis, black titania, methylene blue

Received: 27 May 2026 Revised: 30 June 2026 Accepted: 27 September 2026

INTRODUCTION

Organic pollutants pose a major threat to the environment and it has been reported that they account for more than 70% of pollutants in industrial effluents.[1,2] These pollutants can have long term health impacts on local populations as well as regional biosystems, hence trying to eliminate them has become a critical issue in wastewater treatment and reutilization.[1] Of the various methods aimed at removing these pollutants from the environment, catalytic degradation is emerging as a promising route and photocatalysis is among the frontrunners. Photocatalysis requires light as part of the activation process and importantly, nanomaterials, which serve as the catalysts. Although various strategies have been reported for the synthesis of nanomaterials, e.g. sol-gel, co-precipitation, and hydrothermal synthesis, solution combustion (SCS) synthesis has emerged as a particularly attractive approach due to its ability to form nanoscale materials.[3] The basic principle of SCS is derived from the field of propellants and sol-gel chemistry. SCS was found to be an efficient method for the synthesis of nanomaterials which have typically been used in the production of ceramic powders and semiconductors.[3] Among these, semiconductor materials based on TiO_2 have attracted much attention in photocatalytic applications.[4]

TiO_2 possesses favourable properties such as efficient photoactivity, high photostability, low cost and non-toxicity that have resulted in its widespread use as a photocatalyst, particularly for environmental and energy applications. However, the major limitation associated with TiO_2 is its wide bandgap (3.2 eV), that restricts its activation to only the UV region of the spectrum. This poses a problem for the use of solar power as an alternative energy source since solar energy only consists of about 5% UV radiation. This inability to utilise broad spectrum solar radiation results from its electronic band structure. As a result, there have been various efforts to engineer the bandgap of TiO_2 to extend its optical activation range. The most common and effective modification strategy is through the introduction of heteroatoms into the lattice of TiO_2 which alters the electronic structure enabling visible light activation.[5] However, another method to improve optical activity is to reduce the oxide to form black titania.

Since the discovery of black TiO_2 in 2011, the enhanced optical, electronic and photocatalytic properties of the material have generated much interest.[6,7] Unlike typical modification strategies of TiO_2 such as doping or coupling, black TiO_2 has been reported to exhibit a disordered surface with a crystalline core. Black or coloured TiO_2 has been reported to form from either the reduction of TiO_2 or the oxidation of low valence state Ti species. The reported reductants used for the synthesis of black TiO_2 are hydrogen gas, hydrides, organic reductants, metal reductants and high energy particle reduction. The most common synthesis of black TiO_2 has been via hydrogen treatment. In this case, hydrogen treatment refers to a reduction of TiO_2 at the surface by hydrogen gas with increased temperatures and pressures. This type of hydrogen treatment does not form metallic Ti, but instead forms various defects in the crystal structure of TiO_2. The most common defects to form are oxygen vacancies, Ti^{3+} centres and Ti-H bonds. The majority of black TiO_2 defects are generated on the surface of the particle, however, there are reports of defects occurring in the bulk structure, likely because of the higher temperatures used. It is clear that the various types of defects that occur in black TiO_2 are a result of the varying synthesis methods. Therefore, it can be stated that the physico-chemical properties of black TiO_2 are dependent upon the properties and purity of the white TiO_2 precursor, as well as important reduction parameters such as time, temperature and pressure.[8,9]

The effect of temperature and time are parameters that have been explored previously, typically by using hydrogen flow or annealing in hydrogen and inert gas mixtures. Leshuk et al. conducted one such study whereby TiO_2 nanoparticles were treated with pure H_2 at 20 bar for 24 hours at different temperatures (250 °C, 350 °C and 450 °C). Through the photocatalytic degradation of methylene blue (MB), it was found that the degradation rate had decreased as a result of increasing the hydrogenation treatment temperature, and the sample

*To whom correspondence should be addressed
Email: mahomeda1@ukzn.ac.za

ISSN 1996-840X Online / South African Chemical Institute / http://saci.co.za/journal
© The Author(s) Published under a Creative Commons Attribution 4.0 International Licence (CC BY 4.0)
https://doi.org/10.17159/0379-4350/2026/v80se1a30

treated at 450 °C had a 67% decrease in its specific surface area compared to the un-hydrogenated control [10]. A similar investigation by Wang et al. demonstrated that high temperatures did not result in any significant changes to the bandgap of TiO_2.[11]

In an effort to counteract the detrimental effects of high temperature treatment for the synthesis of black TiO_2, Lu et al. used room temperature coupled with high pressure H_2 treatment (35 bar). However, it was found that due to the lack of high temperatures, the black TiO_2 only began to form after 15 days of treatment. The particles displayed good visible light absorption, a crystalline-disordered core shell structure and enhanced photocatalytic activity, therefore providing a basis to show that high pressure hydrogen treatment can be highly beneficial for the synthesis of black TiO_2 albeit at the expense of time.[12]

Black TiO_2 has previously been synthesised using a variety of precursor TiO_2 materials, including hydrothermally synthesised TiO_2, sol–gel synthesised TiO_2, and commercially available TiO_2. In this study, solution combustion synthesis (SCS) was identified as an effective approach for producing TiO_2 with high phase purity. Despite its advantages, the use of SCS-derived TiO_2 as a precursor for black TiO_2 has not been extensively explored and therefore represents a promising and novel synthetic route to black titania. Combustion-synthesised TiO_2 is particularly attractive as a precursor material due to its inherent defect structures, high surface area, high crystallinity, and excellent phase purity, all of which may contribute to enhanced photocatalytic performance after hydrogen reduction.

Herein we report the effect of hydrogen pressure on the physical, chemical and electronic properties of SCS TiO_2. Following the work of Leshuk et al. and Wang et al. as discussed previously, mild temperature conditions were maintained for this study.[10,13] A temperature of 200 °C was selected to reduce the photocatalysts without significantly diminishing the surface area and thus inhibiting the photoactivity of the materials. The effect of pressure was investigated by the use of incremental increases in the hydrogen pressure treatment which were atmospheric conditions, 10 bar, 30 bar and 50 bar, thus providing a substantial range of low, medium and high pressure conditions over a reaction period of 2 days. The effect of reaction time was also investigated by maintaining a constant pressure of 50 bar over 6 days for one of the catalysts showing good activity at the less severe conditions. The selection of the most suitable SCS derived TiO_2 for the black titania catalytic application was done after testing the precursor materials synthesised by different fuels for photocatalytic activity.

The photocatalytic activity was explored by applying the materials to the degradation of methylene blue (MB). Four catalysts were prepared using urea (U), glycine (G), ethylene glycol (EG) and citric acid (CA) to establish their activity prior to reduction. The catalysts were named after the fuel used, to give U-TiO_2, EG-TiO_2, CA-TiO_2 and G-TiO_2 for urea, ethylene glycol, citric acid and glycine respectively. U-TiO_2, after being found to be most catalytically active, was chosen to synthesise black titania by hydrogen reduction and the materials produced were designated with the pressure at which reduction took place over a period of 2 days e.g. U-10, the catalyst was reduced at 10 bar for 2 days. The U-50-6 catalyst was reduced at 50 bar for 6 days.

EXPERIMENTAL

Materials and Instrumentation

Fourier-Transform Infrared Spectroscopy

Fourier-transform infrared spectroscopy (FTIR) of the samples was conducted in the attenuated total reflectance (ATR) mode, using a Perkin Elmer Spectrum 100 spectrometer (Perkin Elmer, USA). Approximately 50 mg of sample was used for each analysis, with the use of a solid sample accessory. The analyses were done in the wavenumber range from 400-4000 cm^{-1}.

Thermogravimetric Analysis

Thermogravimetric analysis (TGA) of the samples was done using a Thermo Analyser SDT Q600 instrument (TA Instruments, USA). Approximately 10 mg of the sample was used for analysis. The temperature range used for analysis was 25-1000 °C with a ramp rate of 10 °C/min under air flow.

Scanning Electron Microscopy

The Zeiss Ultra Plus Field Emission Gun SEM (Zeiss, Germany) was used to conduct scanning electron microscopy (SEM) imaging. Prior to analysis, samples were coated on double sided carbon tape and placed on an aluminium stub. These were then inserted into a Quorum Q150 ε vacuum evaporator (Quorum technologies, UK) to coat the samples in gold. The Joel JSM-6100 (Joel Ltd., Japan) was used for electron dispersive X-ray (EDX) analysis in conjunction with SEM analysis.

BET Surface Area and Nitrogen Physisorption

Nitrogen physisorption and BET surface area measurements were conducted with a Micromeritics Tri-star 3030 (Micromeritics, USA) instrument. Samples were degassed using a Vacprep 061 instrument (Micromeritics, USA). Weighed samples were heated at 90 °C for 1 hour, followed by an increase in temperature to 150 °C for 1 hour and then overnight at 200 °C under nitrogen flow (Afrox, 99.99%). Once the samples were cooled, analyses for surface area measurements were conducted at -196 °C using liquid nitrogen. Surface area measurements were based on the Brunauer-Emmett-Teller (BET) method and pore size distributions were evaluated by the Barrett-Joyner-Halenda (BJH) method.

High Resolution Transmission Electron Microscopy

High resolution transmission electron microscopy (HRTEM) was done using a JOEL HRTEM 2100 instrument (Joel Ltd., Japan). Prior to analysis, the samples were prepared by sonication in absolute ethanol for 10 minutes. Formvar coated copper grids were dipped into the sample solution and left to dry before being placed in the instrument for analysis.

X-ray Diffraction

X-ray diffraction measurements were performed using a Bruker AXS D8-Advance diffractometer (Bruker, Germany) with a Cu-Kα radiation ($\lambda K\alpha_1$=1.5406 Å). Scans were obtained within a 2θ range of 10-80° with a scan step rate of 0.034° under ambient conditions.

Raman Spectroscopy

Raman spectra of the samples were obtained in the 180 ° configuration using a System 1000 Renishaw Raman spectrometer (Renishaw, UK). The spectrometer was equipped with a microscope and CCD detector. Analysis was carried out using an Ar+ laser with an incident wavelength of 514 nm. Samples were analysed as powders under ambient conditions.

UV-diffuse reflectance spectroscopy

UV-diffuse reflectance spectroscopy was done using a high resolution HR 2000 Ocean Optics spectrophotometer (Ocean Optics, USA) containing a tungsten halogen lamp between wavelengths of 200-1000 nm. The samples were analysed on a 1/4" SS Dip Probe, T300-RT-UV Vis and barium sulphate was employed as the reference material prior to each analysis.

Photoluminescence Spectroscopy

A Perkin Elmer LS-55 Fluorescence spectrometer (Perkin Elmer, USA) was used to obtain photoluminescence (PL) spectra, in conjunction

with a LS-55 solid probe accessory. An excitation wavelength of 320 nm was used for the analysis of all the samples. Operational parameters such as excitation slit, emission slit and scan speed were set as 5.0 nm, 0.0 nm and 100 nm min^{-1} respectively.

Photocatalytic experiments

For each photocatalytic reaction 100 mL of a 5 ppm MB solution was poured into the reaction vessel using a volumetric flask. Thereafter, 50 mg of catalyst was weighed on an analytical mass balance and added to the reactor vessel. The vessel was then placed on the magnetic heating plate and secured into place using clamps. The reaction was left to stir at 500 rpm in the dark for 15 minutes using a large sized magnetic stirrer bar. Thereafter, the lamp (UV or UV-visible) was inserted into the double walled immersion chamber and connected to a 250 W socket. The immersion chamber was then inserted into the reaction vessel and secured into place by Teflon super tape sealing the reaction vessel. The cabinet doors were closed and the lamp switched on for a specific duration of time using the built-in timer. At chosen irradiation intervals, 5 mL of solution was collected and centrifuged to remove catalyst particles for further study. In order to estimate the residual concentration of the dye solution, the UV–vis absorbance was measured with a Shimadzu UV-3600 UV–vis spectrophotometer (Shimadzu, Japan). Prior to photocatalytic testing, standard solutions of MB were prepared in the range of 0 to 5 ppm in 0.5 ppm increments for calibration. During timed intervals of the photocatalytic reaction, 3 mL of the centrifuged sample, in a cuvette, was analysed by the spectrophotometer using Shimadzu UV probe software. A change in the characteristic absorption peaks of MB at 663 nm was monitored at different irradiation times to measure the degradation rate.

General Procedure

Synthesis of Titanyl Nitrate

Titanyl nitrate was synthesised following the method of hydrolysis and nitration. Titanium isopropoxide (Sigma Aldrich, 97%) underwent hydrolysis by continuous stirring in ice-cold double distilled water to form titanium hydroxide. This waxy white solid precipitate was then vacuum filtered to remove excess water. Titanium hydroxide was then dissolved in nitric acid (Associated Chemical Enterprises, 70%) to form titanyl nitrate as described by Challagulla et al.[14]

Solution Combustion Synthesis of TiO_2

In a typical solution combustion synthesis procedure, stoichiometric amounts of titanyl nitrate and fuel were combined in a 1:1 metal-to-fuel ratio in a 1000 mL borosilicate beaker. Subsequently, 40 mL of double-distilled water was added, and the mixture was stirred until a homogeneous solution was obtained. The reaction vessel was then placed in a programmable muffle furnace at room temperature. The furnace temperature was ramped to 80 °C over 2 h and maintained at this temperature for a further 2 h to facilitate solvent evaporation and gel formation. Thereafter, the temperature was increased to 350 °C over 2 h and held for an additional 2 h to initiate the combustion process. After cooling to room temperature, the resulting materials were collected and ground into a fine powder using a mortar and pestle. The powdered samples were then transferred into a quartz calcination boat and placed in a tube furnace for calcination under a constant flow of air (Afrox). Calcination was carried out at 500 °C for 6 h. The final materials were subsequently collected and stored in glass vials for further analysis and application. The following fuels were used, ethylene glycol (Alfa Aesar, 99%), urea (Alfa Aesar, 99-100%), glycine (Sigma Aldrich, 99%) and citric acid (Sigma Aldrich, 99.5%).

Hydrogen treatment of the urea SCS catalyst to produce black titania

For the hydrogen treatment of TiO_2, 1 mL of ground catalyst powder (urea synthesised catalyst) was packed between two layers of glass wool in a stainless-steel reactor tube. The remainder of the tube was filled with carborundum, as well as glass wool at the beginning and end points of the reactor tube. Once the system was completely sealed, nitrogen gas (Afrox, 99.99%) was allowed to flow through the system to displace any air. The introduction of hydrogen (Afrox, 99.99%) was done through a successive blending process, as shown in Table 1, while maintaining a constant flow rate of 25 mL min^{-1} equating to a GHSV of 1500 h^{-1}. At 100% H_2 concentration, the pressure was adjusted accordingly while maintaining the gas flow using a back-pressure regulator. The temperature was maintained at 200 °C and the reduction was left to continue over 2 or 6 days whilst maintaining a constant temperature and pressure. Once the reaction was complete, the reactor system was depressurised and left to cool to room temperature. The reactor assembly was carefully dismantled allowing for the sample to be removed from the reactor tube and stored in a desiccator. All reduced catalysts were characterized.

RESULTS AND DISCUSSION

Fourier-transform Infrared Spectroscopy

The Fourier-transform infrared (FTIR) spectroscopic analysis of all four combustion-synthesised TiO_2 materials were carried out to verify the chemical structure in the frequency range of 400 - 4000 cm^{-1} as shown in Figure S1 (supplementary). It is observed that all four SCS photocatalysts display the same characteristic features regardless of the type of fuel used. Commercially obtained TiO_2 (com-TiO_2) shown in black, was also analysed, as reference. The stretching mode of the metal oxide skeleton occurs in the region between 400 - 800 cm^{-1}. The prominent band at 700 cm^{-1} represents the stretching mode of Ti-O and Ti-O-Ti bonds.[15] Another feature observed in the low frequency region was the band at 1635 cm^{-1} which correlates with the bending vibration of adsorbed molecular water or OH groups present on the surface of TiO_2.[16] The bands between 1400 - 2900 cm^{-1} can be attributed to the stretching modes of carbonyl groups (C=O) as well as aliphatic C-H and CH_2 stretches as a result of unreacted organic residue.[17] Corresponding to the bending vibration of OH groups at 1635 cm^{-1}, the stretching vibrations of strongly bonded OH groups were also visible in the 3200 – 3600 cm^{-1} region with different intensities, for each fuel.[16]

In an effort to gain further insight into the chemical changes as a result of hydrogen treatment, the FTIR spectra of the H_2 treated urea catalysts were also examined, the results of which are shown in Figure 1. All catalysts maintain the same characteristic spectral features as the precursor U-TiO_2, with the exception of U-50-6. The catalysts

Table 1 Gas blends for reduction (30-minutes for each transition)

Transition	Gas Ratio/%	Flowrate ratio (N_2, ml/min: H_2, ml/min)
1	100 % N_2 : 0% H_2	25 : 0
2	90% N_2 : 10% H_2	22.5 : 2.5
3	80% N_2 : 20% H_2	20 : 5
4	70% N_2 : 30% H_2	17.5 : 7.5
5	60% N_2 : 40% H_2	15 : 10
6	50% N_2 : 50% H_2	12.5 : 12.5
7	25% N_2 : 75% H_2	6.25 : 18.75
8	0% N_2 : 100% H_2	0 : 25

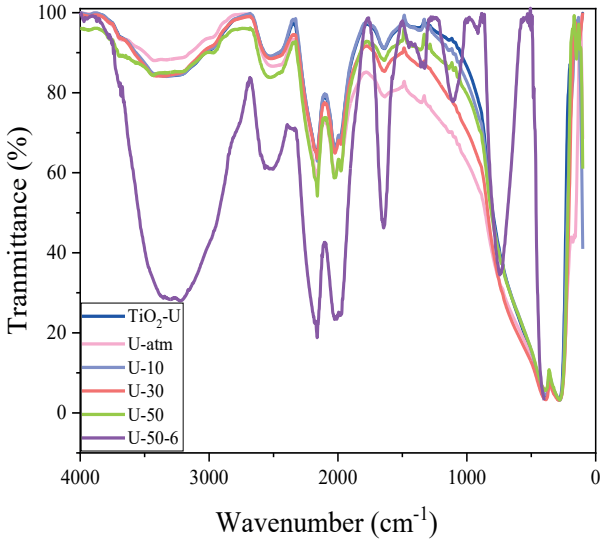


Figure 1. Fourier-transform infrared spectra of H_2 treatment TiO_2 catalysts

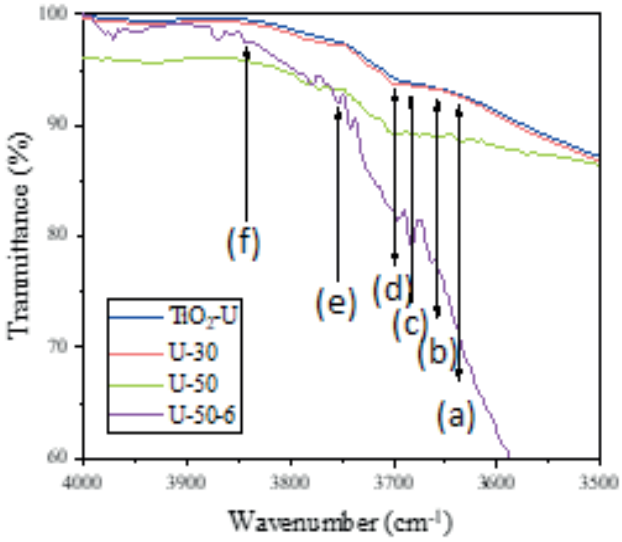


Figure 2. Fourier-transform infrared spectra within the 3500-4000 cm^{-1} region

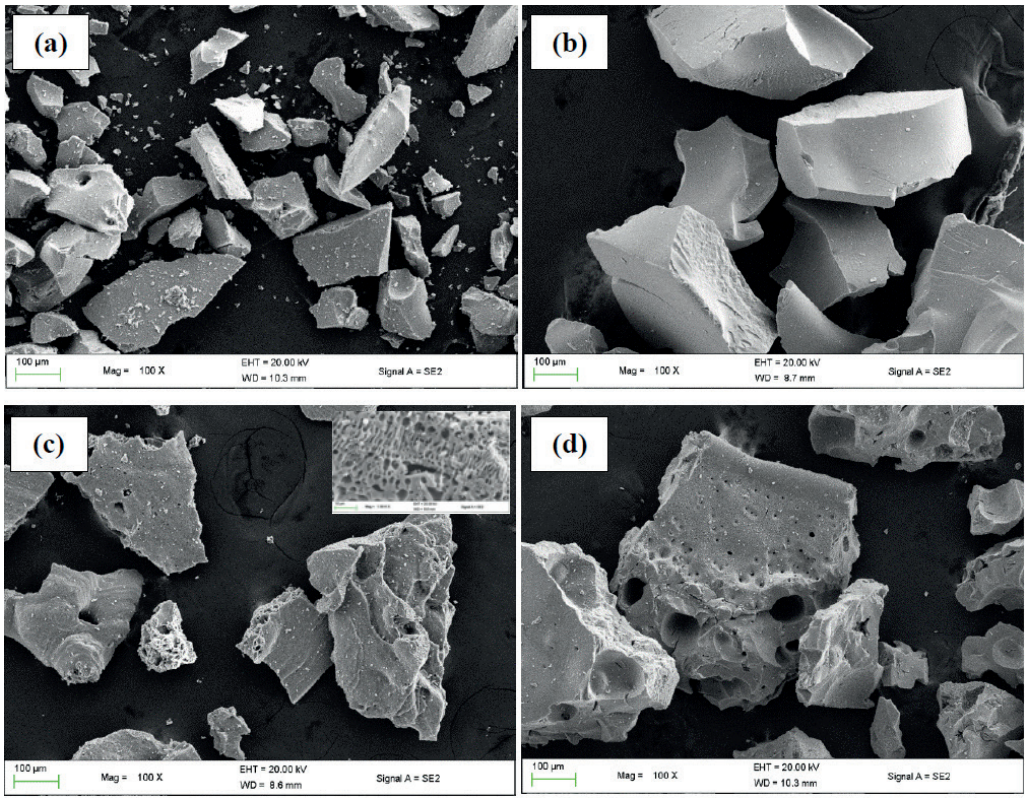


Figure 3. SEM images of **(a)** U-TiO_2, **(b)** EG-TiO_2, **(c)** G-TiO_2 and **(d)** CA-TiO_2

also show similar peak intensities as compared to U-TiO_2, except for U-50-6 which shows a significantly higher intensity than all the other catalysts. The characteristic bands are similar to those discussed for the previously mentioned SCS catalysts. The FTIR spectrum of U-50-6 reveals some additional peaks at 727 cm^{-1} and 1100 cm^{-1} which were attributed to silicon carbide contamination.

The FTIR spectra in the region of 3500-4000 cm^{-1} for the unreduced and selected reduced catalysts are shown in Figure 2. In this enlarged region of the spectrum, several new peaks were identified, particularly for samples U-50 and U-50-6, albeit with very low intensities, and also for U-30. The spectrum of the U-TiO_2 catalyst, also displayed in the figure, showed no discernible bands in this region, indicating that a change in the chemical structure occurred only after hydrogen treatment. The first 3 peaks identified at 3645 cm^{-1} (a), 3670 cm^{-1} (b), and 3685 cm^{-1} (c) are characteristic of tetrahedral coordinated vacancies designated as Ti^{4+}-OH. The last peak at 3700 cm^{-1} (d) is attributed to terminal OH groups. For the synthesis of H-doped black TiO_2, Wang et al. also reported new peaks in this region as a result of hydrogen doping.[18]

A further two peaks at 3750 cm^{-1} (e) and 3840 cm^{-1} (f) were only seen in the FTIR spectra of U-50-6 with strong intensity and in U-50 with very weak intensity, which were attributed to octahedral vacancies and designated as Ti^{3+}-OH.[19]

Scanning Electron Microscopy

In the SEM images of the unreduced catalysts, shown in Figure 3, it can be seen that U-TiO_2 and EG-TiO_2 aggregates consisted of smooth textured and tightly packed particles. G-TiO_2 displayed uniformly distributed holes in the particles as well as cracks. This type of hole structure was seen throughout the material with the holes serving as entrance to pores and channels of various sizes and

orientations (see insert of Figure 3(c)). These pores are in macropore range considering the scale bar of the SEM images. CA-TiO_2 appears to have large particles attached together to form clusters as well as voids. This material is also visibly porous. Reports in literature, where combustion synthesised materials were prepared using either glycine or citric acid as fuel, showed similar textural characteristics. Oshani et al. indicated that the use of urea in the SCS of TiO_2 resulted in smooth flake like material whereas glycine synthesised TiO_2 had a spongy and porous microstucture consistent with what is observed here.[20]

Nitrogen Physisorption and BET surface area analysis

Table 2 gives the BET surface area, pore size and pore volume data of the SCS catalysts as well as the H_2 treated urea catalysts. Commercial titania was included as reference. The data shows that there is a significant difference in the surface characteristics of the materials as a result of using different fuels, and in addition, the un-reduced SCS catalysts exhibit significantly higher surface areas than the commercial sample. The large difference in surface area caused by the fuels can be attributed to differences in combustion flame temperature and the amount of gases released during the reaction for the respective fuels. G-TiO_2 and CA-TiO_2 display very narrow pore diameters and low pore volumes because of cavitation, resulting in lower surface areas. The microstructural observations from the SEM images are in good agreement with the specific surface area measurements. As seen in Table 2, the BET surface area of the U-TiO_2 catalyst was 116 $m^2 g^{-1}$ prior to hydrogen treatment. However, when treated with hydrogen, a decrease in the surface area of U-atm (urea catalyst reduced at atmospheric H_2-pressure) to 94 $m^2 g^{-1}$ was observed. Pressure treatment at 10, 30 and 50 bar over 2 days and 50 bar over 6 days, did not cause the surface area of the catalysts to decrease much further. It was observed however, that there was a slight increase in the pore size as the severity of the hydrogen treatment was increased. The pore volume remained the same for the reduced catalysts. From the N_2 adsorption-desorption isotherms (Figures S2 and S3, Supplementary), it can be observed that all the catalysts display a type H1 hysteresis loop classification, indicating a narrow range of uniform mesopores, except for G-TiO_2 and CA-TiO_2 which exhibited a type H2(a) hysteresis.[21] Little change in the hysteresis was observed after the reduction of U-TiO_2; however, a decrease in the amount of N_2 adsorbed was observed, concomitant with a decrease in surface area, shown in Table 2.

Table 2. BET surface area, pore size and pore volume of the SCS and H_2 treated TiO_2 catalysts

Catalyst	BET Surface area/ mg^{-1}	Pore size/ nm	Pore volume/ $cm^3 g^{-1}$
Com-TiO_2	8.6	5.5	0.01
G-TiO_2	31	2.9	0.02
CA-TiO_2	52	3.2	0.06
EG-TiO_2	73	4.4	0.12
U-TiO_2	116	5.2	0.22
U-atm	94	6.5	0.02
U-10	95	6.6	0.02
U-30	94	6.7	0.02
U-50	93	6.9	0.02
U-50-6	92	7.4	0.02

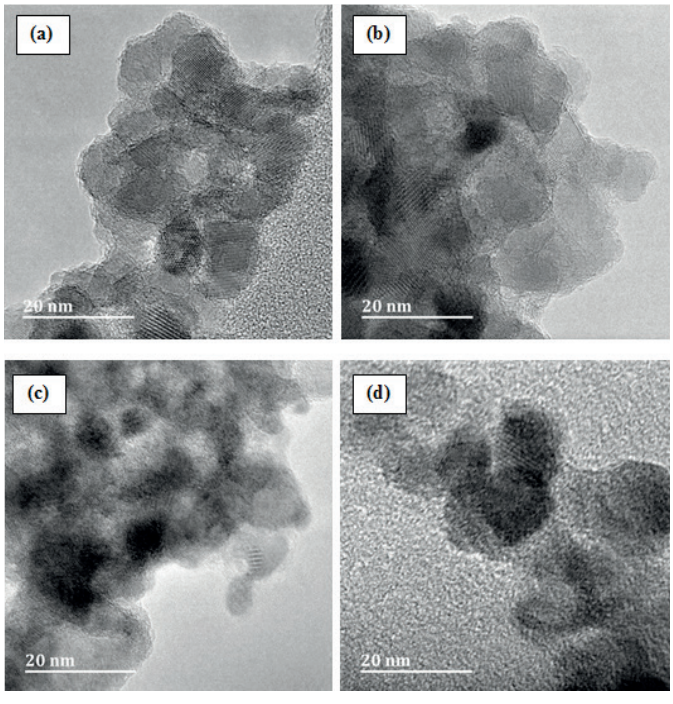


Figure 4. HRTEM images of combustion synthesised **(a)** U-TiO_2, **(b)** G-TiO_2, **(c)** EG-TiO_2 and **(d)** CA-TiO_2

High Resolution Transmission Electron Microscopy

The particle morphology was studied using HRTEM, as shown in Figure 4. All the materials consisted of crystalline nanoparticles, as evidenced by the presence of well-defined lattice fringes in the HRTEM images. The measured interplanar spacing of 0.36 nm corresponded to the d-spacing of the (101) plane of anatase TiO_2. The nanoparticle sizes ranged from 7 to 14 nm. No lattice fringes or structural features associated with the rutile phase were observed in any of the four catalysts.

X-ray Diffraction

The X-ray diffractograms of the combustion synthesised TiO_2 as well the H_2 treated TiO_2 recorded in a 2θ range from 10 – 80° is given in Figure 5. In respect of the unreduced catalysts, it can be seen that the diffraction patterns of all four catalysts show no significant differences in their key features, irrespective of the fuel used. The catalysts exhibit narrow and well-formed peaks indicative of their crystalline nature. The most intense peak, appearing at 25.3° was attributed to the (101) plane of anatase. The diffractogram showed other peaks at 2θ angles of 37.7°, 48°, 53.8°, 55.1° and 62.6° which could be referenced to (004), (200), (105), (211) and (204) planes of the anatase phase of TiO_2 (JCPDS card file no. 78-2486), respectively.

Peaks corresponding to the rutile or the brookite phase of TiO_2 were not observed, confirmed by HRTEM and Raman spectroscopy even though SCS has been reported to form rutile due to the high temperatures of the combustion reaction.[22] The absence of the rutile phase was beneficial to this study owing to the higher photocatalytic activity of anatase compared to rutile.[23]

The X-ray diffractograms were also used to determine the average crystallite size of the TiO_2 nanoparticles. From the resulting diffractograms in Figure 5, the average crystallite size was calculated from the line broadening of the anatase (101) diffraction peak using the Scherrer equation, shown in Equation 1:

$$D = \frac{0.9\lambda}{\beta\cos\theta} \qquad \text{(Equation 1)}$$

where D is the average nanocrystallite size (nm), λ is the X-ray wavelength (1.542 Å), β is the full-width at half-maximum (FWHM) intensity (in radians), and θ is the Bragg angle of the peak of interest. The average crystallite size for all the combustion synthesised catalysts were found to be between 11-14 nm (Table 3), which are in reasonable agreement with the crystallite size measured by HRTEM although the latter showed a wider range, but still favouring smaller

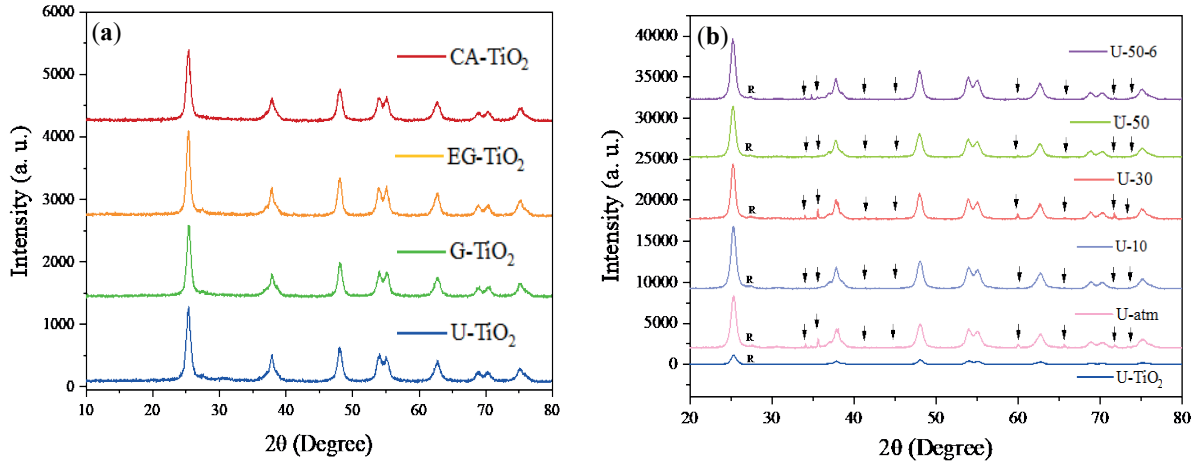


Figure 5. X-ray diffractogram of **(a)** solution combustion synthesised TiO_2 photocatalysts and **(b)** hydrogen treated TiO_2

Table 3. Crystallite size, peak position and FWHM of SCS catalysts

Photocatalyst	Peak Position 2θ/ °	FWHM β/ °	Crystallite size *D*/nm
U-TiO_2	25.35	0.73745	11.54
G-TiO_2	25.40	0.66416	12.82
EG-TiO_2	25.33	0.60791	14.00
CA-TiO_2	25.34	0.68508	12.42

Table 4. Crystallite size, peak position and FWHM of H_2 treatment catalysts

Photocatalyst	Peak Position 2θ/°	FWHM β/°	Crystallite size *D*/nm
U-TiO_2	25.350	0.73745	11.54
U-atm	25.335	0.70123	12.14
U-10	25.319	0.68030	12.51
U-30	25.277	0.66421	12.81
U-50	25.262	0.65356	13.02
U-50-6	25.269	0.63093	13.49

crystallite size. The changes in the crystalline structure of TiO_2 as a result of hydrogen pressure treatment was also studied by XRD.

Figure 5(b) shows the X-ray diffractograms for the hydrogen treated catalysts as well as the pre-cursor U-TiO_2 catalyst. The peaks of the H_2 treated catalysts showed good intensity indicating that they maintained a crystalline nature after H_2 treatment. The diffractograms show dominant peaks at 2θ of 25.3°, 37.7°, 48°, 53.8°, 55.1° and 62.6° which could be referenced as (101), (004), (200), (105), (211) and (204) planes of the anatase phase of TiO_2 respectively. This indicates that after high pressure hydrogen treatment, whether over 2 or 6 days, the materials still maintain their anatase phase. It is however interesting to note that after the hydrogen treatment the most intense peak ascribed to the (110) plane of the rutile phase appeared at about 2θ = 27° but with an intensity that made it difficult to integrate. The position of the peak has been denoted on the diffraction pattern with "R." The XRD pattern also revealed that all H_2 treated catalysts contained different quantities of silicon carbide as an impurity, denoted with black arrows.[24] The crystallite size of the hydrogen treated catalysts, given in Table 4, was also calculated from the line broadening of the anatase (101) diffraction peak using the Scherrer equation. The data shows that the crystallite size increased with increasing hydrogen pressure and treatment time.

The peak attributed to the (101) plane of anatase for U-TiO_2 as well as the H_2 treated catalysts is shown in Figure 6. It can be observed that as the hydrogen pressure and reduction time was increased, indicating an increase in the severity of the hydrogen treatment, a

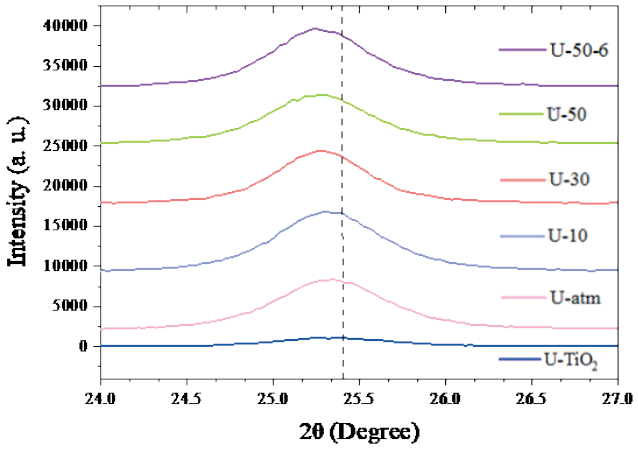


Figure 6. Peak shift (101) of H_2 treated catalysts

shift of this peak occurred to lower 2θ values from a reference value of 25.35° 2θ for U-TiO_2, indicating a slight increase of the d-spacing associated with this set of planes. The increase in the d-spacing could be due to lattice defects induced by the formation of Ti^{3+} ions and oxygen vacancies.[25]

An additional diffraction peak at 2θ = 35°, assigned to the (110) plane of Ti_2O_3, was observed in Figure S4 (Supplementary Information). This observation suggests the formation of Ti^{3+} species induced by the high-pressure hydrogen treatment [26]. Notably, this peak was detected only for the U-50-6 sample, which underwent treatment at 50 bar for 6 days, indicating that prolonged hydrogen treatment may promote a higher concentration of Ti^{3+} species and/or Ti_2O_3 formation.

Raman Spectroscopy

The Raman spectra of all four un-reduced SCS synthesised catalysts as well as the reduced urea catalysts are given in Figure 7. The Raman spectrum of the anatase phase consists of six Raman active modes which are A_{1g}, $2B_{1g}$ and $3E_g$. These occur at 144 cm^{-1} (E_g), 197 cm^{-1} (E_g), 399 cm^{-1} (B_{1g}), 513 cm^{-1} (A_{1g}), 519 cm^{-1} (B_{1g}), and 639 cm^{-1} (E_g) with A_{1g} and B_{1g} modes appearing as a doublet band in the spectrum.[27] The active E_g modes at 144 cm^{-1} and 197 cm^{-1} typically correspond to Ti-Ti interactions within a unit cell and the O-O covalent bonding interactions are found within the 246-351 cm^{-1} region. E_g and B_{1g} bands are a result of the symmetric stretching vibration of O-Ti-O bonds and symmetric bending of vibrations of O-Ti-O bonds respectively. The A_{1g} mode corresponds to antisymmetric bending vibrations of Ti-O-Ti in TiO_2. The E_g band at 144 cm^{-1} is the most intense and well resolved mode due to external symmetric

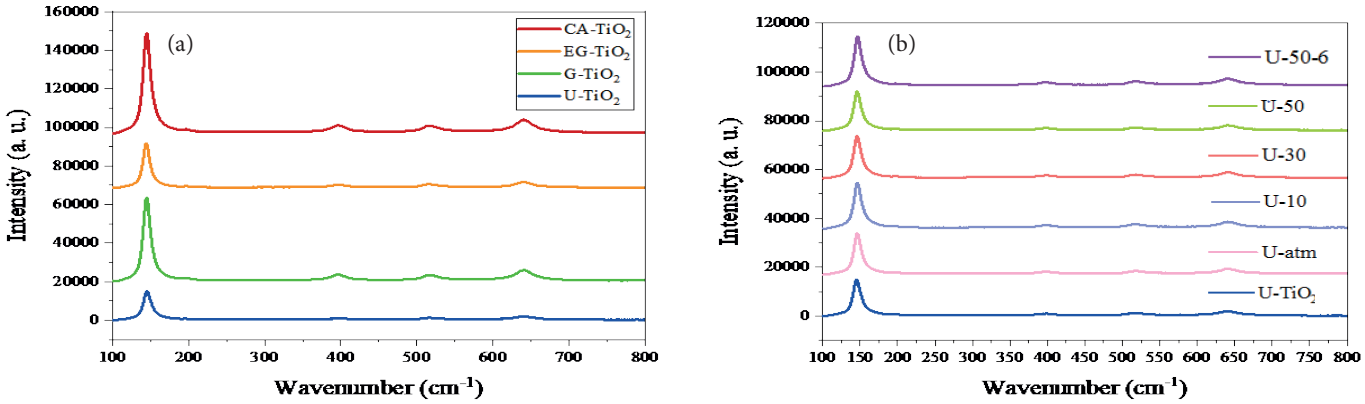


Figure 7. Raman spectra of **(a)** combustion synthesised and **(b)** H_2 treated TiO_2 catalysts

vibrations further confirming the formation of long range order anatase phase.[28] After high pressure hydrogen treatment, all catalysts appeared to have maintained the anatase phase with no indication of the formation of the rutile phase, although trace amounts of this phase were detected by X-ray diffraction.

The lowest frequency vibrational mode, E_{1g} appearing at 144 cm^{-1}, was investigated for changes in crystallinity and non-stoichiometry for the reduced black titania catalysts, as shown in Figure 8. It can be seen that as the severity of the hydrogen treatment increased, the peak's maximum appears to be shifted towards higher wavenumbers in relation to the unreduced catalyst (U-TiO_2). There was also a slight peak broadening effect noticed with increasing hydrogen pressure and reaction time. A similar trend of peak broadening and peak shift of the E_{1g} Raman modes towards the higher wave number compared to the pristine anatase TiO_2 nanotubes was reported for the partially reduced anatase TiO_2 nanotubes by Zhang et al. This is indicative of the formation of defects in the crystalline structure, such as oxygen vacancies and non-stoichiometry, as a result of the high-pressure hydrogen treatment.[29]

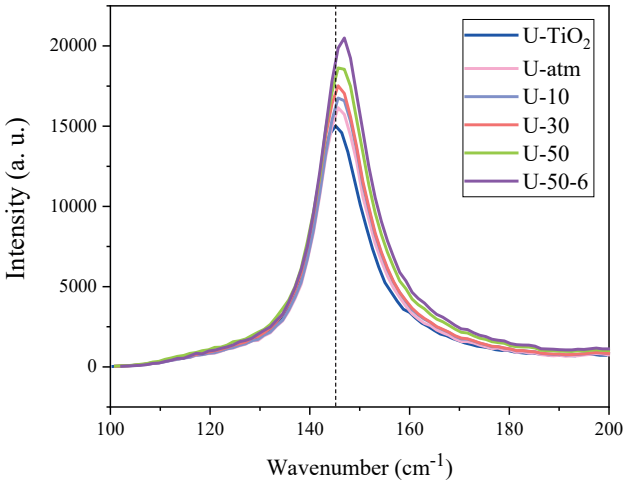


Figure 8. E1g band of the catalysts.

UV-Visible Diffuse Reflectance Spectroscopy

The UV-DRS spectra of the SCS photocatalysts and the commercial catalyst is given in Figure S5 (Supplementary). The commercial TiO_2 is observed to exhibit a steep absorption edge located at 395 nm indicative of the excitation of electrons from the valence band (O 2p states) to the conduction band (Ti 3d states). For all the combustion synthesised catalysts, this absorption edge was red shifted towards the visible region of the spectrum. Since absorbance is influenced by the size and shape of a particle, the red shift of the absorption edge could be attributed to the different crystallite sizes of the combustion synthesised TiO_2 as a result of the fuel. A shift of the absorption edge towards higher wavelengths indicates a more efficient utilisation of light for photocatalysis. Challagulla et al. also reported a change in the bandgap energy in the SCS of anatase TiO_2 as a result of the fuel used.[14] The UV-visible DRS absorbance spectrum of combustion synthesised anatase using glycine as a fuel and commercial Degussa P-25 was compared and it was found that the combustion synthesised TiO_2 had two optical absorbance maxima at 570 nm and 476 nm that were 1.62 and 2.35 fold higher than the commercial Degussa P-25 absorbance thresholds respectively.[30]

The effect of the high-pressure hydrogen treatment on the optical absorbance in the UV, visible and near infrared regions are shown in Figure S6 (Supplementary). Within the UV region of the spectra, between 200-400 nm, the hydrogen treated TiO_2 catalysts exhibits a much higher UV light response compared to the untreated U-TiO_2 and the commercial TiO_2. The absorption edge of the hydrogen treated TiO_2 catalysts display an increasing red-shift with increased hydrogen treatment as compared to the untreated U-TiO_2. However, the most pronounced effect of hydrogen pressure treatment was seen in the visible and near IR region, between 400-1000 nm. All four hydrogen-treated TiO_2 samples exhibited enhanced absorbance as compared to the untreated U-TiO_2 and the commercial TiO_2 within the visible region and IR regions. The U-50-6 sample exhibited the highest increase in absorbance in the visible and IR range compared to all the other catalysts. A time-based absorbance spectrum of P25 under 35 bar H_2 was monitored over a period of 20 days at room temperature, and it was reported that significant changes in the visible region were only found for samples treated after 15-20 days.[12] However, in the present work, a significant increase in absorption in the visible region was observed, at lower pressures and after just 2 days.

The optical band gaps of the combustion synthesised TiO_2 catalysts as well as the H_2 treated catalysts were calculated from the Tauc plots in Figure S7 (Supplementary). The bandgap value for the commercial TiO_2 was calculated as a reference in both plots. Com-TiO_2 yielded a bandgap energy value of 3.2 eV, which is in accordance with literature values for the bandgap of anatase TiO_2.[31] The bandgaps of the combustion synthesised TiO_2 materials were 2.93 eV, 2.87 eV, 2.86 eV and 2.85 eV for U-TiO_2, G-TiO_2, CA-TiO_2 and EG-TiO_2, respectively. The variation in bandgap energies can be attributed to the varying crystallinity of the catalysts as a result of the fuel used in the combustion reaction. The bandgaps of the hydrogen treatment TiO_2 catalysts were smaller than that of the pre-treated U-TiO_2 catalyst. The bandgaps of the hydrogen treatment TiO_2 catalysts decreased with increasing pressure treatment as shown in Table 5. It can be reasoned that the decreased bandgap, as a result of high pressure hydrogen treatment, enables a greater efficiency for photoactivation in the visible and IR regions of the EM spectrum.

In order to elucidate the theoretical band structure of the H_2 treated catalysts, the valence band edge potential (E_{VB}) and the conduction

Table 5. Band gap energy and the band edge potentials, E_{CB} and E_{VB} of H_2 treated catalysts

Catalyst	VB Edge Potential /eV	CB Edge Potential /eV	Bandgap Energy /eV
U-TiO_2	2.745	-0.185	2.93
U-atm	2.715	-0.155	2.87
U-10	2.705	-0.145	2.85
U-30	2.695	-0.135	2.83
U-50	2.680	-0.120	2.80
U-50-6	2.630	-0.070	2.70

band edge potential (E_{CB}) of the photocatalysts were determined using Equations 2 and 3:

$$E_{CB} = \chi - E_e + 0.5E_g \quad \text{(Equation 2)}$$

where, E_{CB}, χ and E_e represent the conduction band edge potential, the absolute electronegativity of the semiconductor and the energy of free electrons on the hydrogen scale taken as 4.5 eV, respectively. The valence band edge potential was calculated using Equation 3:

$$E_{VB} = E_{CB} + E_g \quad \text{(Equation 3)}$$

The E_g values estimated from the Tauc plot, as well as the calculated valence and conduction band edge potentials are given in Table 5. A decreasing bandgap energy and VB edge potential, as well as an increasing CB edge potential was observed as the hydrogen severity increased. These results of the high-pressure hydrogen treatment, suggests a greater efficiency for photoactivation in the visible and IR regions of the EM spectrum.

Photoluminescence spectroscopy

Photoluminescence spectroscopy is an important technique used for the study of ion-trapping, migration and transfer of charge carriers thus enabling a deeper understanding of the electron/hole relationship within the semiconductor. PL spectral analysis can be used to study oxygen vacancy states, surface states, colour centres and interstitial states thus forming a defect profile.[32] The PL emission spectra appearing in Figure 9(a) shows that there is a significant difference in the emission intensities of the SCS TiO_2 catalysts as an inherent effect of the fuel used. Lower PL intensity suggests suppressed electron–hole recombination and improved charge carrier separation efficiency. U-TiO_2 displays the lowest emission intensity, followed by EG-TiO_2 and CA-TiO_2, with G-TiO_2 showing the highest emission intensity of all four catalysts. The variation in emission intensities between the catalysts is indicative of defects in the crystal lattice or surface, which can be attributed to the changes in the crystalline nature of the catalyst because of the fuels used during the synthesis.

Figure 9 (b) shows the PL spectrum of U-TiO_2 as well as the catalysts after reduction with H_2. The emission intensities of the hydrogen treated catalysts appear significantly lower than that of U-TiO_2, with U-50-6 showing the lowest emission intensity. The results demonstrate that increasing the extent of H_2 treatment reduces the PL emission intensity, suggesting a lower rate of electron–hole recombination and consequently, a longer lifetime of photogenerated charge carriers.

The dominant features of the PL spectra can be related directly or indirectly to the presence of oxygen vacancies. The first peak occurring just before 400 nm corresponds to the bandgap energy emission. The highest intensity emission, centered at 421 nm was as a result of self-trapped excitons due to hole capturing by electrons localised within the TiO_6 octahedra.[32] The peak at 445 nm represents surface states which are located within the bandgap and can trap excited state electrons, effectively contributing to emissions at higher wavelengths.[33] The defects present in black TiO_2 such as H-doping, V_0 and Ti^{3+} self-doping allow them to act as trapping

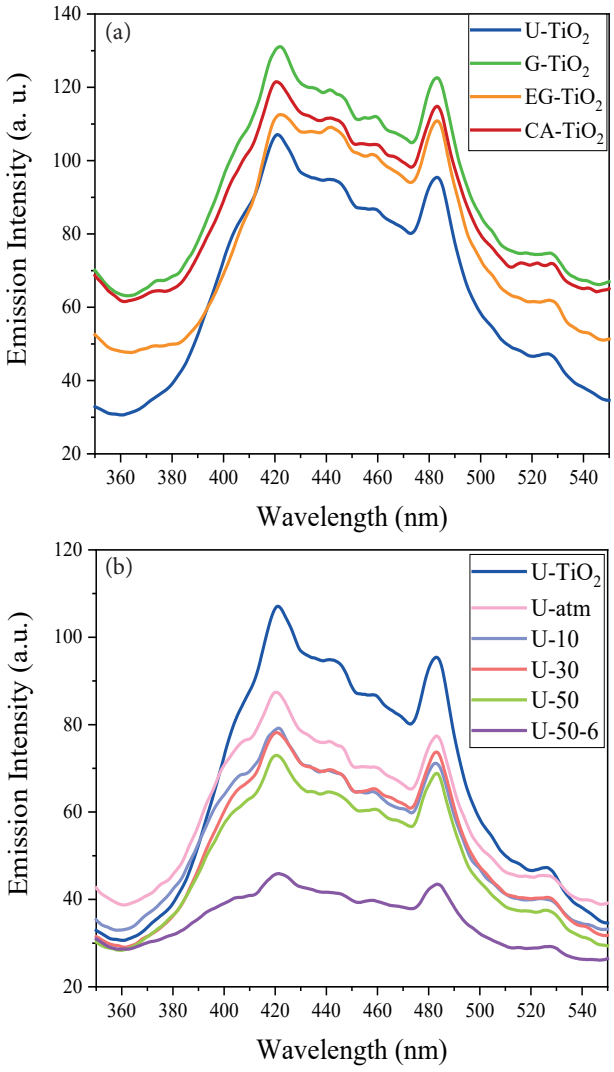


Figure 9. Photoluminescence emission spectrum of (a) SCS and (b) hydrogen treated TiO_2

sites for photogenerated charge carriers thereby inhibiting the rate of recombination of charge carriers.[34] The emission at 460 nm was attributed to shallow and deep surface traps associated with the Ti^{3+} state.[35] The second highest emission peak at 485 nm was ascribed to the charge transfer transition from Ti^{3+} in Ti 3d orbital to the nearby oxygen anion in O 2p orbitals.[36] The last emission peak at 528 nm has been assigned to the different surface oxygen vacancies.[32] Therefore, the difference in PL emission intensities was due to the inherent effect of the extent of hydrogen treatment which resulted in a higher quantum efficiency. Wang et al. synthesised black TiO_2 through aluminium reduction in a two-zone furnace and reported significantly lower photoluminescence emission intensities which was attributed to the formation of $V_{0.}$[37]

Photocatalysis

The photocatalytic activity of the TiO_2 photocatalysts for the degradation of methylene blue (MB) using UV and UV-Visible radiation is shown in Figure 10. The control reactions, that is without catalyst, as well as with the commercial TiO_2, for the degradation of MB, is given in Figure S8 in the supplementary information. When irradiated with UV light (Figure 10(a)), U-TiO_2 showed 100% degradation of MB in a time of 60 min. EG-TiO_2 was the only other catalyst to completely degrade MB within the allocated reaction time (100 min), however, at a slower rate, compared to U-TiO_2.

G-TiO_2 and CA-TiO_2 demonstrated lower photocatalytic activity. These results indicate that U-TiO_2 gave the best photocatalytic activity

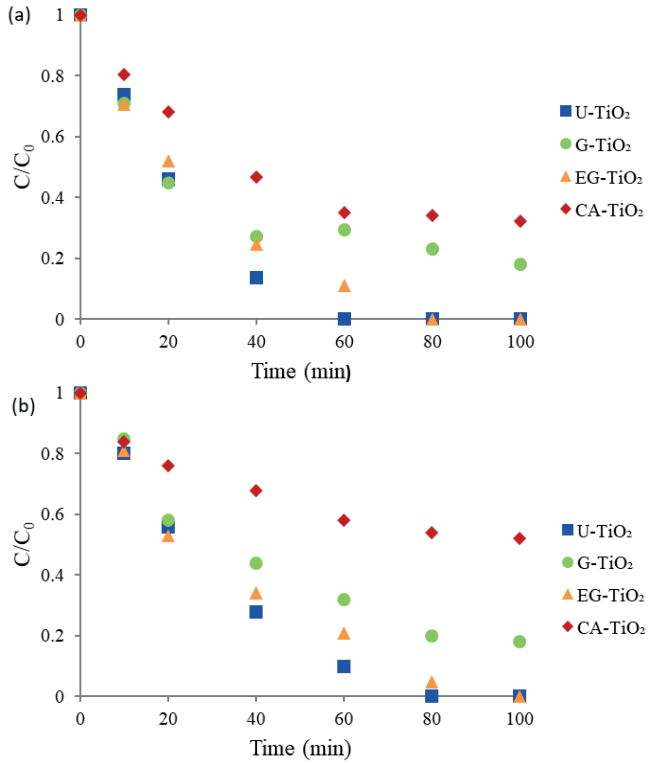


Figure 10. **(a)** UV and, **(b)** UV-visible photocatalytic degradation of MB using SCS un-reduced TiO_2.

for the degradation of MB under UV light. When UV-vis light was used (Figure 10 (b)), a similar trend was observed in respect of activity, however, the efficiency was reduced as compared to UV light only. U-TiO_2 took about 80 min to degrade MB completely under UV-vis light compared to when only UV light was used.

The kinetic data for the reactions, based on pseudo first-order kinetics, are given in Figure S9 and in Table S1 (Supplementary) which shows that U-TiO_2 had the highest rate of MB degradation when either source of light was used. This was followed by EG, G and CA. The high photocatalytic efficiency of U-TiO_2 can be attributed to its high surface area, low recombination rate, interstitial defects, and high concentration of surface hydroxyl groups. G-TiO_2 exhibited low k_{app} values as compared to EG-TiO_2 and U-TiO_2, however when these values were normalised with the respective surface areas of each catalyst, it was seen that G-TiO_2 has the capacity to perform well, however its low surface area hinders its photocatalytic activity indicating that surface area is also an important parameter for these photocatalytic reactions. This was not the case for CA-TiO_2 since this catalyst displayed the lowest rate constants before and after being normalised with its surface area for both the UV and UV/visible light reactions. CA-TiO_2 also displayed the lowest density of surface hydroxyl groups, therefore this, coupled with its rather high rate of charge carrier recombination, based on the PL data, as well as low surface area, contributed to the poor activity of this catalyst. The high activity of U-TiO_2 prompted the hydrogen treatment study and the photocatalytic results for the hydrogen treated U-TiO_2 catalyst are given in Figure 11 and Figure 12 with UV and UV-visible light respectively.

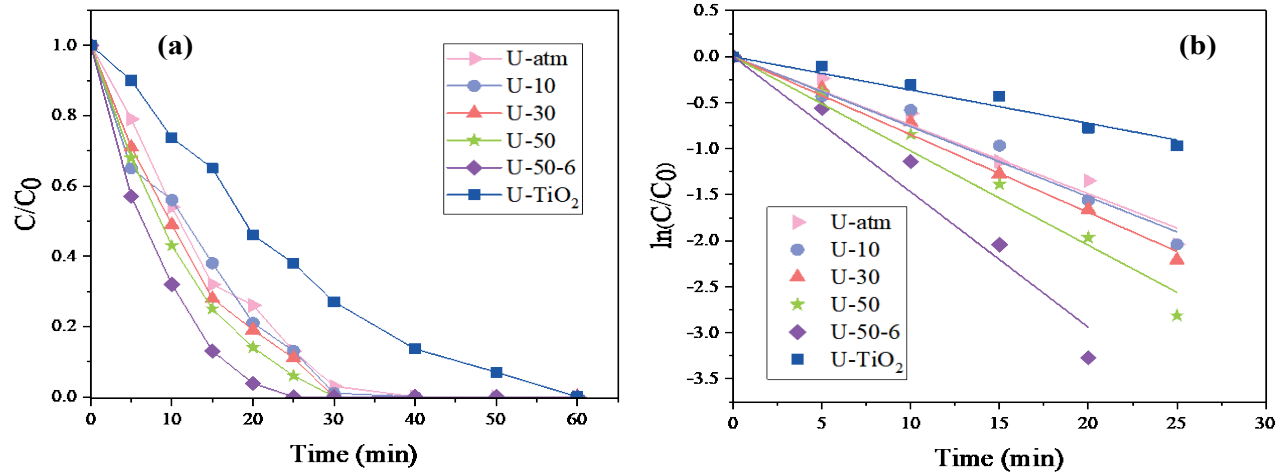


Figure 11. **(a)** UV photocatalytic degradation of MB and **(b)** Plot of $\ln(C/C_0)$ versus time for the photocatalytic degradation rate of MB for H_2 treated photocatalysts

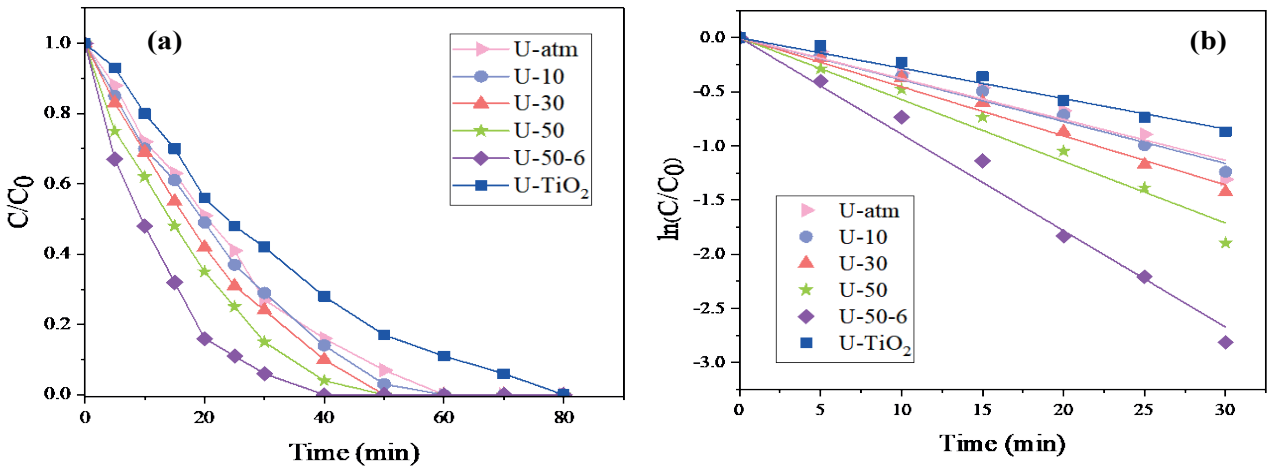


Figure 12. **(a)** UV-visible photocatalytic degradation of MB and **(b)** Plot of $\ln(C/C_0)$ versus time for the photocatalytic degradation rate of MB for H_2 treated photocatalysts

The UV photocatalytic activity of the H_2 treated catalysts as compared to the untreated U-TiO_2 in the degradation of MB is given in Figure 11 (a). It can be observed that all the H_2 treated photocatalysts were able to completely degrade the MB solution in a time of between 30 - 40 min as compared to 60 minutes for untreated U-TiO_2. The high-pressure treated photocatalysts (50 bar) performed slightly better than the low-pressure and atmospheric pressure treated catalysts. At 20 min the 6-day treated catalyst, labelled as U-50-6, achieved 96.2% degradation of MB and 100% degradation within 25 min. These results were significantly higher than the 2 day treated catalysts. Figure 11 (b) shows a significant increase in the reaction rate when comparing the pre-treated U-TiO_2 to the H_2 treated materials. There were also slight differences in the photocatalytic rates between the different H_2 treated photocatalysts, with the exception of U-50-6, which had a significantly higher rate of MB degradation.

The activities of the H_2 treated photocatalysts when using UV-visible light are shown in Figure 12. (a). U-50-6 was able to degrade 84% of the MB solution within the first 20 min of the reaction, as compared to U-TiO_2 which only degraded 44% of MB during the same time period. The other H_2 treated catalysts also performed well and displayed photocatalytic efficiencies of 100% between 50 - 60 min. The k_{app} values (Table S2, Supplementary) indicate that the H_2 treated samples performed considerably better than the unreduced U-TiO_2 catalyst under both UV and UV-visible light conditions. Following a similar trend to the UV light results, the UV-visible k_{app} values increased with increasing pressure treatment. The most active catalyst, U-50-6 had a k_{app} value of 0.0891 min^{-1}, which was 3.2 times higher than U-TiO_2. The data in Table S2 demonstrate the effectiveness of the H_2 treatment, as the H_2-treated catalysts exhibited superior performance under UV–visible irradiation compared to U-TiO_2 under UV irradiation alone. Although the optimised hydrogen-reduced TiO_2 catalyst demonstrated enhanced photocatalytic activity, its reusability and long-term stability were not evaluated in the present study, representing a limitation that is hoped to be addressed in future work.

The basic mechanism proposed for the photocatalytic degradation of MB by the hydrogen treated TiO_2 follows a similar route to that of the untreated TiO_2. Figure 13 shows a schematic of the photogenerated charge separation of U-50-6 as a result of its reduced bandgap and defect or impurity levels in its bandgap due to the hydrogen treatment. The hydrogen treatment resulted in a reduction in the optical band-gap energy, as determined from the Tauc analysis, together with enhanced absorption in the visible-light region. Consequently, under UV–visible irradiation, photons with sufficient energy can promote electrons from the valence band to the conduction band, generating photogenerated electron–hole pairs. The photogenerated holes can oxidise adsorbed water molecules or surface hydroxyl species to form hydroxyl radicals (•OH), while conduction-band electrons can reduce dissolved oxygen to form superoxide radicals (O_2^{-}) which can subsequently produce hydroperoxy radicals (HOO•) on protonation and thereafter highly reactive •OH radicals after dissociation. The degradation of MB is strongly influenced by the formation of (•OH) radicals over the surface of the hydrogen treated materials.[18] In the hydrogen treated materials, the formation of oxygen vacancies (Vo) and Ti^{3+}, proposed to introduce defect sites within the TiO_2 structure, may facilitate the trapping and transfer of photogenerated charge carriers and thereby suppress electron-hole recombination.[38] Additionally, the defect sites may contribute to enhanced sub-bandgap adsorption following the hydrogen treatment. These combined modifications provide a plausible explanation for the enhanced photocatalytic degradation of MB observed under both UV and visible-light irradiation for the hydrogen treated TiO_2 materials. In the absence of ROS-specific experiments, the contribution of individual species, including •OH and O_2^{-}, cannot be conclusively established. Accordingly, the ROS-mediated pathway described above is presented as a proposed mechanism based on the observed physicochemical properties and photocatalytic behaviour of the catalysts, together with established photocatalytic pathways reported for TiO_2.[39]

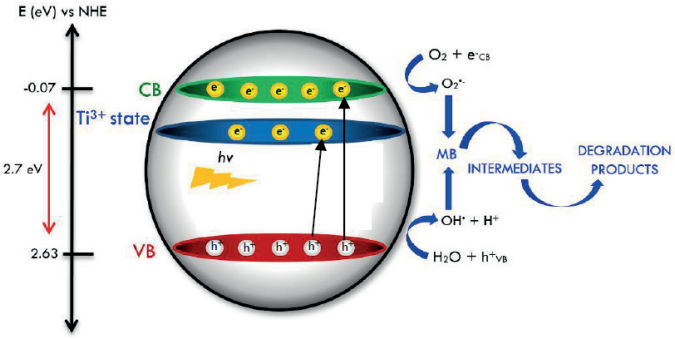


Figure 13. Photogenerated charge separation of U-50-6 and its photocatalytic process.

A comparison of U-50-6, the high-pressure hydrogen-treated catalyst, with other black TiO_2-based photocatalysts reported for the degradation of methylene blue is presented in Table S3 in the Supplementary Information. The referenced studies employ a range of black TiO_2 synthesis strategies, which differ substantially from the hydrogen-treatment approach used in the present work. Based on the apparent degradation rate constants (k_{app}), U-50-6 exhibited a comparatively high degradation rate relative to the other catalysts included in the comparison. Although direct comparison should be interpreted with caution due to differences in irradiation and other experimental conditions, the limited number of studies reporting the photocatalytic degradation of methylene blue using black TiO_2 makes this comparison appropriate for placing the performance of U-50-6 within the context of the currently available literature. In addition, the well-established white TiO_2 photocatalyst, Degussa P25, and a Pd-doped black TiO_2 catalyst were included in Table S3 as reference materials for comparison.

CONCLUSION

In this study, TiO_2 was synthesised using the method of solution combustion synthesis as a single step process. The fuels urea, glycine, ethylene glycol and citric acid were used for the synthesis of U-TiO_2, G-TiO_2, EG-TiO_2 and CA-TiO_2, respectively. It was reasoned from XRD analysis that the materials were predominantly anatase, which was also confirmed from Raman and HRTEM analyses, however, the possible presence of a minor rutile phase in the urea and ethylene glycol synthesised samples cannot be excluded; although its quantity could not be reliably quantified. The Raman analysis suggested defects may have arisen in the urea derived materials based on the low intensity and broadened peaks. In comparison to all the synthesised catalysts, U-TiO_2 exhibited the most promising characteristics such as the highest surface area of 116 $m^2\ g^{-1}$, the smallest crystallite size (11.54 nm) obtained from XRD, highest concentration of surface hydroxyl groups, well-formed pore structure and lowest photoluminescence intensity. As a result, for the photocatalytic study, the urea synthesised TiO_2 material (U-TiO_2) gave the highest activity for UV and UV/visible photocatalytic degradation of methylene blue. The U-TiO_2 was then subjected to a series of hydrogen reduction experiments. FTIR analysis revealed the formation of tetrahedral coordinated vacancies designated as Ti^{4+}-OH and octahedral coordinated vacancies designated at Ti^{3+}-OH for U-50 and U-50-6 with stronger intensity. XRD analysis revealed the formation of the Ti_2O_3 phase in U-50-6, further confirming the presence of the Ti^{3+} species. The broadening and blueshift of the E_g mode in the Raman spectrum were revealed to be as a result of oxygen vacancy formation. The changes to the properties of the material due to hydrogen treatment resulted in enhanced MB degradation for the reduced catalysts compared to the unreduced catalyst.

SUPPLEMENTARY INFORMATION

The supporting information contains additional figures and tables containing characterisation data, such as FT-IR spectra, adsorption-desorption data, UV spectra and Tauc plots; as well as tabulated kinetic data.

ACKNOWLEDGEMENTS

We are grateful to the microscopy and microanalysis unit (MMU) at the University of KwaZulu-Natal for their assistance with TEM and SEM imaging. We would also like to extend our gratitude to the National Research Foundation (NRF) for funding this research (Grant No: 116249).

AUTHOR CONTRIBUTIONS

Pooja Phillip: Conceptualization, methodology, synthesis, investigation, formal analysis, catalytic studies, data curation, visualization, writing – original draft. Sooboo Singh: supervision, writing – review and editing, funding acquisition, resources. Holger Friedrich: supervision, resources. Abdul S. Mahomed: Supervision, conceptualization, writing – review and editing, validation.

DECLARATION OF COMPETING/FINANCIAL INTERESTS

The authors declare that they have no known competing financial interests or personal relationships that could have appeared to influence the work reported in this paper.

DECLARATION OF GENERATIVE AI AND AI-ASSISTED TECHNOLOGIES

Authors declare that no generative AI or AI-assisted technologies were used in the writing of the manuscript.

ORCID IDS

Pooja Phillip: https://orcid.org/0000-0001-6746-5265
Sooboo Singh: https://orcid.org/0000-0001-5765-1013
Holger B. Friedrich: https://orcid.org/0000-0002-1329-0815
Abdul S. Mahomed: https://orcid.org/0000-0002-1255-5500

REFERENCES

1. Lu JY, Bu ZQ, Lei YQ, Wang D, He B, Wang J, Huang WT. Facile microwave-assisted synthesis of Sb2O3-CuO nanocomposites for catalytic degradation of p-nitrophenol. J Mol Liq. 2024;409:125503. https://doi.org/10.1016/j.molliq.2024.125503
2. Liang S, Feng X, Li X, Wang Z, Miao K, Feng G, Luo X. Catalysis of nonstoichiometric Mn–Co spinel oxides in effective peroxymonosulfate activation: Structure–activity relationship and flow-through organic wastewater treatment. Sep Purif Technol. 2026;397:138142. https://doi.org/10.1016/j.seppur.2026.138142
3. Varma A, Mukasyan AS, Rogachev AS, Manukyan KV. Solution Combustion Synthesis of Nanoscale Materials. Chem Rev. 2016;116(23):14493–14586. https://doi.org/10.1021/acs.chemrev.6b00279
4. Li Y, Cheng H, Jiang W, Xie J, Xie Y, Gao J, Ding Y. Efficient photocatalytic CO2 reduction over copper-containing polyoxometalate grafted on blue TiO2 catalyst. Chem Eng J. 2026;541:177930. https://doi.org/10.1016/j.cej.2026.177930
5. Daghrir R, Drogui P, Robert D. Modified TiO2 for environmental photocatalytic applications: a review. Ind Eng Chem Res. 2013;52(10):3581–3599. https://doi.org/doi:10.1021/ie303468t
6. Chen X, Liu L, Peter YY, Mao SS. Increasing solar absorption for photocatalysis with black hydrogenated titanium dioxide nanocrystals. Science. 2011;331(6018):746–750. https://doi.org/10.1126/science.1200448
7. Sahoo SS, Mansingh S, Babu P, Parida K. Black titania an emerging photocatalyst: review highlighting the synthesis techniques and photocatalytic activity for hydrogen generation. Nanoscale Adv. 2021;3(19):5487–5524. https://doi.org/10.1039/D1NA00477H
8. Liu X, Zhu G, Wang X, Yuan X, Lin T, Huang F. Progress in black titania: a new material for advanced photocatalysis. Adv Energy Mater. 2016;6(17):1600452. https://doi.org/10.1002/aenm.201600452
9. Hayat M, Ahmed T, Saleem A, Gul I, Noor U, Bukhari A, Yasir M, Nasir A. Black titania: An emerging engineered material with advanced synthesis strategies and applications. Inorg. Chem. Commun. 2026;189:116763. https://doi.org/10.1016/j.inoche.2026.116763
10. Leshuk T, Parviz R, Everett P, Krishnakumar H, Varin RA, Gu F. Photocatalytic activity of hydrogenated TiO2. ACS Appl Mater Interfaces. 2013;5(6):1892–1895. https://doi.org/10.1021/am302903n
11. Wang G, Wang H, Ling Y, Tang Y, Yang X, Fitzmorris RC, Wang C, Zhang JZ, Li Y. Hydrogen-treated TiO2 nanowire arrays for photoelectrochemical water splitting. Nano Lett. 2011;11(7):3026–3033. https://doi.org/10.1021/nl201766h
12. Lu H, Zhao B, Pan R, Yao J, Qiu J, Luo L, Liu Y. Safe and facile hydrogenation of commercial Degussa P25 at room temperature with enhanced photocatalytic activity. RSC Adv. 2014;4(3):1128–1132. https://doi.org/10.1039/c3ra44493g
13. Wang W, Ni Y, Lu C, Xu Z. Hydrogenation temperature related inner structures and visible-light-driven photocatalysis of N–F co-doped TiO2 nanosheets. Appl Surf Sci. 2014;290:125–130. https://doi.org/10.1016/j.apsusc.2013.11.013
14. Challagulla S, Roy S. The role of fuel to oxidizer ratio in solution combustion synthesis of TiO2 and its influence on photocatalysis. J. Mater. Res. 2017;32(14):2764–2772. https://doi.org/10.1557/jmr.2017.244
15. Chen Y, Kang K, Yoo K, Jyoti N, Kim J. Cause of slow phase transformation of TiO2 nanorods. J Phys Chem C. 2009;113(46):19753–19755. https://doi.org/10.1021/jp9086442
16. Lopez T, Moreno J, Gomez R, Bokhimi X, Wang J, Yee-Madeira H, Pecchi G, Reyes P. Characterization of iron-doped titania sol–gel materials. J Mater Chem. 2002;12(3):714–718. https://doi.org/10.1039/B105724N
17. Zhang J-Y, Boyd IW, O'sullivan B, Hurley P, Kelly P, Senateur J-P. Nanocrystalline TiO2 films studied by optical, XRD and FTIR spectroscopy. J Non-Cryst Solids. 2002;303(1):134–138. https://doi.org/10.1016/S0022-3093(02)00973-0
18. Wang Z, Yang C, Lin T, Yin H, Chen P, Wan D, Xu F, Huang F, Lin J, Xie X. H-doped black titania with very high solar absorption and excellent photocatalysis enhanced by localized surface plasmon resonance. Adv Funct Mater. 2013;23(43):5444–5450. https://doi.org/10.1002/adfm.201300486
19. Kumar PM, Badrinarayanan S, Sastry M. Nanocrystalline TiO2 studied by optical, FTIR and X-ray photoelectron spectroscopy: correlation to presence of surface states. Thin Solid Films. 2000;358(1-2):122–130. https://doi.org/10.1016/S0040-6090(99)00722-1
20. Oshani F, Hashemi S. Effect of various fuels on structure and photocatalytic activity of TiO2 nano-crystalline prepared by microwave-assisted combustion method. Prog. Color Color Coat. 2011;4(2):85–94. https://doi.org/10.30509/pccc.2011.75784
21. Bardestani R, Patience GS, Kaliaguine S. Experimental methods in chemical engineering: specific surface area and pore size distribution measurements—BET, BJH, and DFT. Can. J Chem Eng. 2019;97(11):2781–2791. https://doi.org/10.1002/cjce.23632
22. Chung S-L, Wang C-M. Solution combustion synthesis of TiO2 and its use for fabrication of photoelectrode for dye-sensitized solar cell. J Mater Sci Technol. 2012;28(8):713–722. https://doi.org/10.1016/S1005-0302(12)60120-0
23. Zhang J, Zhou P, Liu J, Yu J. New understanding of the difference of photocatalytic activity among anatase, rutile and brookite TiO2. Phys Chem Chem Phys. 2014;16(38):20382–20386. https://doi.org/10.1039/c4cp02201g
24. Jin G-Q, Guo X-Y. Synthesis and characterization of mesoporous silicon carbide. Micropor Mesopor Mat. 2003;60(1-3):207–212. https://doi.org/10.1016/S1387-1811(03)00378-0
25. Li J, Wu E-H, Hou J, Huang P, Xu Z, Jiang Y, Liu Q-S, Zhong Y-Q. A facile method for the preparation of black TiO2 by Al reduction of TiO2 and their visible light photocatalytic activity. RSC Adv. 2020;10(57):34775–34780. https://doi.org/10.1039/d0ra06784a
26. Li R, Kobayashi H, Guo J, Fan J. Visible-light-driven surface reconstruction of mesoporous TiO2: toward visible-light absorption and enhanced photocatalytic activities. Chem Comm. 2011;47(30):8584–8586. https://doi.org/10.1039/C1CC12464A

27. Ohsaka T, Izumi F, Fujiki Y. Raman spectrum of anatase, TiO2. J Raman Spectrosc. 1978;7(6):321–324. https://doi.org/10.1002/jrs.1250070606
28. Tian F, Zhang Y, Zhang J, Pan C. Raman spectroscopy: a new approach to measure the percentage of anatase TiO2 exposed (001) facets. J Phys Chem C. 2012;116(13):7515–7519. https://doi.org/10.1021/jp301256h
29. Zhang X-Q, Chen J-B, Wang C-W, Liao A-Z, Su X-F. Low-temperature liquid phase reduced TiO2 nanotube arrays: synergy of morphology manipulation and oxygen vacancy doping for enhancement of field emission. Nanotechnology. 2015;26(17):175705. https://doi.org/10.1088/0957-4484/26/17/175705
30. Nagaveni K, Sivalingam G, Hegde M, Madras G. Solar photocatalytic degradation of dyes: high activity of combustion synthesized nano TiO2. Appl Catal B-Environ. 2004;48(2):83–93. https://doi.org/10.1016/j.apcatb.2003.09.013
31. Kumar SG, Devi LG. Review on modified TiO2 photocatalysis under UV/visible light: selected results and related mechanisms on interfacial charge carrier transfer dynamics. J Phys Chem A. 2011;115(46):13211–13241. https://doi.org/10.1021/jp204364a
32. Sarkar A, Khan GG. The formation and detection techniques of oxygen vacancies in titanium oxide-based nanostructures. Nanoscale. 2019;11(8):3414–3444. https://doi.org/10.1039/c8nr09666j
33. Bharad PA, Sivaranjani K, Gopinath CS. A rational approach towards enhancing solar water splitting: A case study of Au–RGO/N-RGO–TiO2. Nanoscale. 2015;7(25):11206–11215. https://doi.org/10.1039/C5NR02613J
34. Zhu G, Yin H, Yang C, Cui H, Wang Z, Xu J, Lin T, Huang F. Black titania for superior photocatalytic hydrogen production and photoelectrochemical water splitting. Chemcatchem. 2015;7(17):2614–2619. https://doi.org/10.1002/cctc.201500488
35. Choudhury B, Bayan S, Choudhury A, Chakraborty P. Narrowing of band gap and effective charge carrier separation in oxygen deficient TiO2 nanotubes with improved visible light photocatalytic activity. J Colloid Interface Sci. 2016;465:1–10. https://doi.org/10.1016/j.jcis.2015.11.050
36. 36. Saini C, Barman A, Banerjee D, Grynko O, Prucnal S, Gupta M, Phase D, Sinha A, Kanjilal D, Skorupa W. Impact of Self-Trapped Excitons on Blue Photoluminescence in TiO2 Nanorods on Chemically Etched Si Pyramids. J Phys Chem C. 2017;121(21):11448–11454. https://doi.org/10.1021/acs.jpcc.7b02218
37. Wang Z, Yang C, Lin T, Yin H, Chen P, Wan D, Xu F, Huang F, Lin J, Xie X. Visible-light photocatalytic, solar thermal and photoelectrochemical properties of aluminium-reduced black titania. Energ Environ Sci. 2013;6(10):3007–3014. https://doi.org/10.1039/c3ee41817k
38. Pan X, Yang M-Q, Fu X, Zhang N, Xu Y-J. Defective TiO2 with oxygen vacancies: synthesis, properties and photocatalytic applications. Nanoscale. 2013;5(9):3601–3614. https://doi.org/10.1039/c3nr00476g
39. Ajmal A, Majeed I, Malik RN, Idriss H, Nadeem MA. Principles and mechanisms of photocatalytic dye degradation on TiO2 based photocatalysts: a comparative overview. RSC Adv. 2014;4(70):37003–37026. https://doi.org/10.1039/c4ra06658h